Received: 16 July 2020 | Revised: 30 September 2020 | Accepted: 23 November 2020

DOI: 10.1002/suco.202000435

TECHNICAL PAPER

fib CEB-FIP WILEY

Numerical study on the mechanical behavior of ultrahigh performance concrete using a three-phase discrete element model

Sebastian Rybczyński[1,2] | **Maksym Dosta**[2] | **Gunnar Schaan**[3] | **Martin Ritter**[3] | **Frank Schmidt-Döhl**[1]

[1]Institute of Materials, Physics and Chemistry of Buildings, Hamburg University of Technology, Hamburg, Germany

[2]Institute of Solids Process Engineering and Particle Technology, Hamburg University of Technology, Hamburg, Germany

[3]Electron Microscopy Unit, Hamburg University of Technology, Hamburg, Germany

Correspondence
Sebastian Rybczyński, Hamburg University of Technology, Germany Institute of Materials, Physics and Chemistry of Buildings, Institute of Solids Process Engineering and Particle Technology, Denickestrasse 15, 21073 Hamburg, Germany.
Email: sebastian.rybczynski@tuhh.de

Funding information
German Research Foundation (DFG), Grant/Award Numbers: SCHM 1473/29-1, RI 1516/2-1, DO 2026/2-1

Abstract

This paper deals with numerical analysis on the mechanical behavior of ultrahigh performance concrete (UHPC) under uniaxial compression. For the modeling of the mechanical behavior of UHPC, the mesh-free discrete element method was applied. To calibrate the model parameters and validate the numerical simulation results, a set of experimental investigations including mechanical tests, microscopy and tomography analysis, were performed. The scanning electron microscopy and polarized light microscopy were used to examine cross sections of UHPC as well as to characterize interfacial transition zone and aggregate in detail. X-ray microtomography analysis was used to obtain information about the nonspherical shape of aggregate and to generate a realistic structural model. Simulation results have shown that the developed model predict stiffness reliably, strength, and breakage pattern of UHPC and shows good agreement with experimental results. Finally, the model has been applied to analyze the main crack initiation in static failure and to investigate the influence of different parameters such as aggregate content as well as aggregate and binder stiffness on the mechanical behavior of UHPC.

KEYWORDS

concrete fracture, discrete element method, SEM, ultrahigh performance concrete

1 | INTRODUCTION

Due to the growing demand for sustainable and lightweight concrete structures, the use of ultrahigh performance concrete (UHPC) is becoming increasingly important. UHPC is an almost ideally brittle material with outstanding mechanical properties. It is an acknowledged fact that the superior properties of UHPC stem from an

Discussion on this paper must be submitted within two months of the print publication. The discussion will then be published in print, along with the authors' closure, if any, approximately nine months after the print publication.

optimization on the basis of the maximum packing density theory.[1,2] Generally, UHPC is manufactured containing a low water to cement ratio (w/c) from 0.14 to 0.24, a high amount of cementitious material, fillers (e.g., quartz powder or fly ash), as well as pozzolanic powders such as silica fume.[3] The optimized particle size distribution, combined with the pozzolanic reactivity of silica (formation of additional calcium silicate-hydrate) leads to a lower porosity within the binder and high strength of the interfacial transition zone (ITZ).[4,5] Furthermore, cement hydration degree in UHPC is as low as 30%, so most of the unhydrated cement also acts as physical filler. Additionally, due to the optimized packing, the strength of UHPC is more strongly influenced by the aggregate than in plain concrete. As a result of this, crack propagation from pores or a weaker ITZ cannot necessarily be assumed as it is the case for plain concrete. Due to this, crack initiation within the UHPC and the localization of possible inhomogeneities is in the focus of current research.

For numerical investigations, the bonded-particle model (BPM) has been used. The BPM is an extension of the discrete element method (DEM), where each pair of particles can be connected with solid bonds.[6,7] By defining a constitutive law for the bonds, different macroscopic effects can be captured such as material hardening or softening. In recent years, BPM has been increasingly used by research groups for the numerical analysis of concrete in 2D and 3D simulations,[8–14] but none of them has been applied the BPM to UHPC. The main disadvantage of 2D simulations is the missing reproducibility of interlocking effects within the structure,[12,13,15] which plays a significant role in concrete structures. The interlocking between aggregate and binder can be reproduced by 3D simulations and even more effectively through the usage of μCT data of single grains. Different techniques including 3D laserscanning[16] and X-ray tomography (μCT)[17–19] have been used in recent years to characterize and analyze the shapes of aggregate in concrete.

Due to the background of the mentioned research, the main purpose of this paper is the illustration of the beneficial usage of DEM for breakage simulations of a special concrete like UHPC. Different microscopy techniques like X-ray tomography, polarized light microscopy (PLM) and scanning electron microscopy (SEM) were used in this context. Furthermore, this paper reports the results of a numerical study, conducted to investigate main crack initiating areas and the potential influence of inhomogeneities (aggregate content and stiffness, binder stiffness) on the mechanical properties of UHPC.

2 | EXPERIMENTAL CHARACTERIZATION

2.1 | Mechanical experiments

Uniaxial compression tests were carried out on cylindrical UHPC and pure binder (concrete composition without coarse aggregate/quartz sand) specimens. All specimens were unmoulded after 24 hr and stored in water for at least 56 days. Afterwards, samples were sawn and ground to the required dimension of h/d = 180/60 mm. An overview of the used concrete composition and the variation for binder specimens is given Table 1.

Finally, mechanical experiments were carried out strain-controlled with a load speed of 0.2 mm/min, while the longitudinal strain was measured by three high-precision inductive displacement transducers. Three specimens of each material were tested, respectively, the experimental results and mechanical properties are shown in Table 2.

2.2 | X-ray microtomography and microscopy for aggregate characterization

To gather statistically robust information on the breakage behavior inside the UHPC structure, automated large-area SEM was used. From the large cylindrical specimens subjected to uniaxial-load testing, a sample block of about $10 \times 10 \times 3$ mm^3 size was sawn. Afterwards, the sample was ground to a sufficiently planar surface, which was

TABLE 1 UHPC composition and single components

Component	Content in kg/m^3	Vol %	UHPC	Binder
Cement (CEM I, 52.5)	795.4	26.16	✓	✓
Silica fume	168.6	7.80	✓	✓
Quartz powder	198.4	7.65	✓	✓
Quartz sand (0.125/0.5)	971	36.58	✓	–
Plasticizer (PCE–3.5 wt% of cem)	27.8	2.70	✓	✓
Water	187.9	19.11	✓	✓

Abbreviation: UHPC, ultrahigh performance concrete.

TABLE 2 Mechanical properties of UHPC and binder obtained from experimental measurements

Specimen	Strength (MPa)	Young's modulus (GPa)	Breakage strain (%)
UHPC I	196	48	4.5
UHPC II	188	46	4.6
UHPC III	196	46	5.1
Binder I	170	38	5
Binder II	174	34	5.7
Binder III	172	36	5.3

Abbreviation: UHPC, ultrahigh performance concrete.

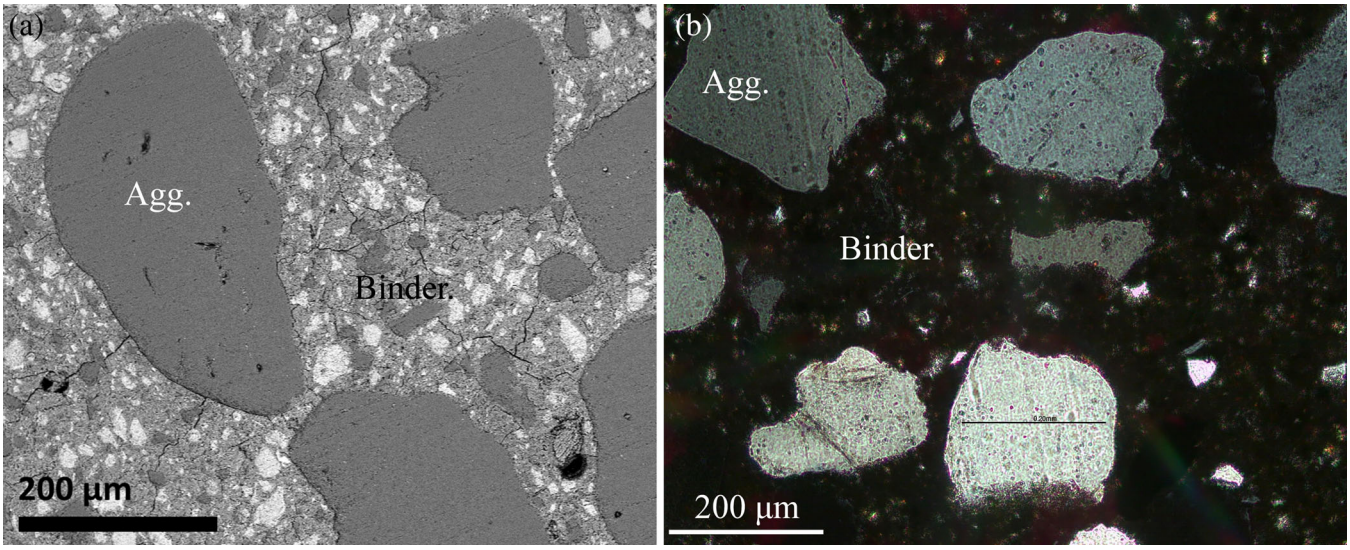

FIGURE 1 (a) SEM image of UHPC cross section, no cracks through aggregate, (b) Light microscopic image of UHPC thin section, crossed polarizers, no phase boundaries within the quartz grains are visible. SEM, scanning electron microscopy; UHPC, ultrahigh performance concrete

then coated with a 10 nm layer of gold. Numerous individual images are acquired automatically using a custom-made routine and then stitched together using an algorithm[20] in ImageJ software package to create a composite large-area image surveying a large portion of the sample surface. To clearly differentiate the constituent components by their respective image contrasts, imaging of backscattered electrons is applied. Figure 1a contains a single image covering ca. 1.18×0.79 mm^2 of the surface of a fractured sample (pixel size ca. 768 nm). Dark-gray, irregularly shaped areas indicate quartz sand (diameter 250 µm) and quartz powder (diameter ca. 20 µm). The cement paste matrix encasing the aggregate grains appears lighter due to its higher content of heavier elements, with unhydrated cement clinker grains appearing very light. The paste is permeated with numerous cracks (due to uniaxial loading and shrinkage cracks caused by the evaporation of water contained in hydrated binder in vacuum). However, cracks directly penetrating the aggregate are not observed. Note that silica fume particles are not visible in the image due to their small size (diameter up to 200 nm).

In addition, PLM analysis of UHPC thin sections was used for further characterization of aggregate. PLM with crossed polarizers showed that no phase boundaries are visible within the quartz grains, see Figure 1b, proving that each aggregate grain is a single crystal. Due to this property and its anisotropic nature, a stiffness of around 90 GPa (parallel to [001]) and 70 GPa (parallel to [100]) could be assumed.[21,22] In order to gather information on the nonspherical shape of aggregate grains, X-ray microtomography (µCT) analysis with a nominal resolution of 3.5 µm has been used and reconstructed to 3D models, see Figure 2a–c.

2.3 | SEM–EDX analysis of ITZ

A potential weaker ITZ would be distinguished from the rest of the binder matrix by an increased concentration of $Ca(OH)_2$ and thus, calcium, which can easily be measured using SEM–EDX analyses. We acquired large-area EDX elemental distribution maps of Si and Ca (Figure 3a), among other elements, and extracted intensity line profiles

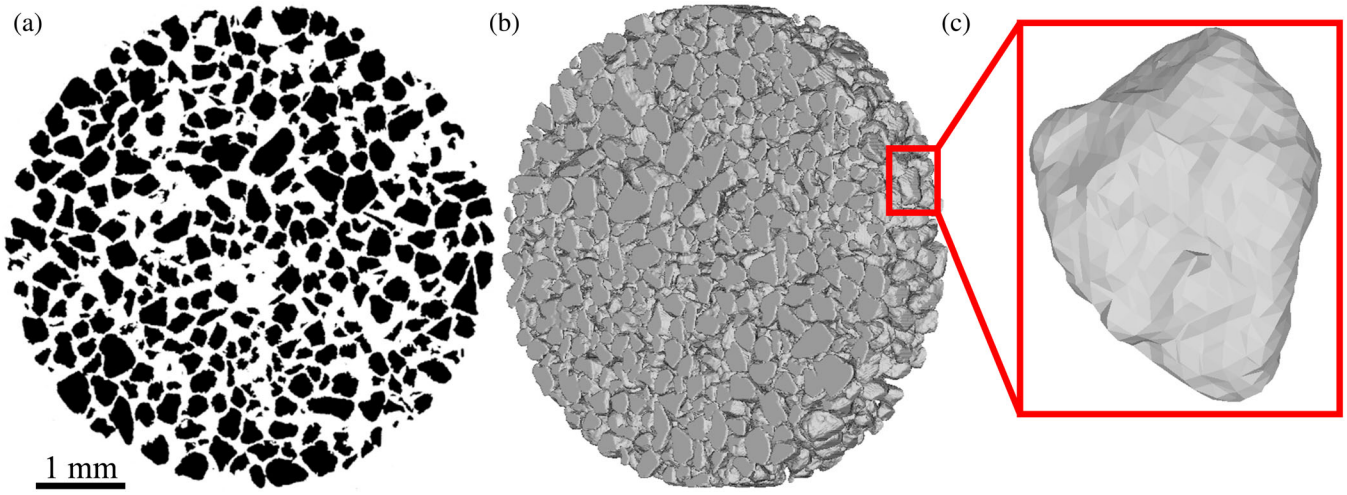

FIGURE 2 X-ray microtomography analysis: (a) Single binary μCT image of measurement, (b) 3D reconstruction of μCT image sequence, (c) 3D model of segmented single aggregate grain

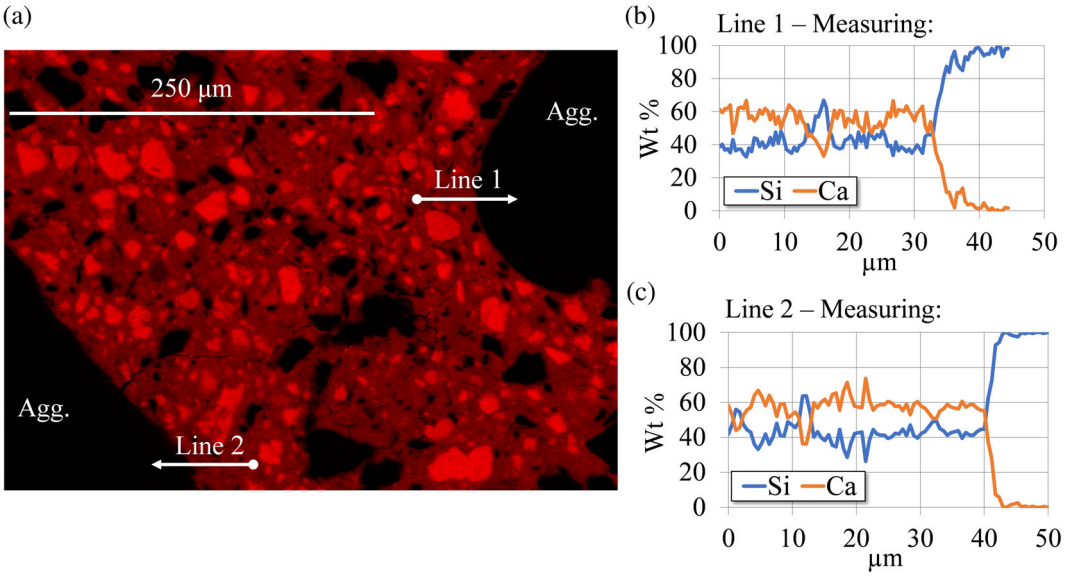

FIGURE 3 (a) SEM–EDX overview of the interface between aggregate and binder and (b) Line scans of Si and Ca concentration with a length of 50 μm

from these maps, see Figure 3b. The profiles were selected to cross the boundary between the binder matrix and a large aggregate grain as well as to cover enough distance (≈ 50 μm) in order to fully contain a potential ITZ.

However, no gradual or abrupt increase in Ca concentration is observed as the profile approaches the aggregate. The only drastic change in concentration occurs as the profile reaches the large aggregate grain, with Ca concentration dropping to nearly zero. Slight fluctuations in the concentration of Ca and Si can arise from small grains of aggregate or unhydrated cement clinker embedded in the binder matrix, either on or just below the sample surface, being covered by the profile. Thus, we conclude that the optimized packing density of the components and the usage of an additional hydraulic component in silica fume contribute to an ITZ with properties identical to the overall binder matrix.

3 | NUMERICAL BACKGROUND

3.1 | The DEM

The DEM is a mesh-free simulation approach to model the mechanical behavior of granular materials. Initially, DEM was developed for the modeling of systems consisting of ideally spherical particles.[23] The motion of particles during simulation is described by Newton's second

law. By this, acceleration for each particle is computed and time-integrated to find its new velocity and position. In addition, contacts between particles and walls (overlaps) are detected and virtual forces are calculated. However, nowadays various extensions of DEM are developed for the modeling of nonspherical particles as multiphase flows or chemical reactions.

All simulations presented in this contribution have been performed in the DEM simulation framework MUSEN.[24] Depending on hardware configuration, MUSEN allows to perform effective simulation for scenes consisting of up to 20 million of discrete objects. The calculations in this system are parallelized for the hybrid CPU–graphic processor unit (GPU) architecture. The contact detection algorithm is executed on the CPU using a multigrid approach[25] combined with linked-cell algorithm and Verlet lists. The calculation of forces and integration of motion is performed on GPU. This strategy reduces computation time significantly and allows numerous simulation studies consisting of large number of discrete objects. The averaged computational time for uniaxial compression test of UHPC sample consisting of 3,965,706 discrete objects was 22 hr for hardware configuration equipped with Intel Xeon Gold 5,118 CPU and NVIDIA Quadro GV100 GPU.

3.2 | Bonded-particle approach

One of the extensions of DEM proposed for modeling of fracture phenomena is the BPM.[7] In BPM, each pair of primary particles can additionally be connected with one or multiple solid bonds. Each particle and each single bond can possess unique geometrical and material parameters that allow to reproduce complex-structured heterogeneous materials. In the present work, a soft-sphere DEM formulation has been used where occurring interparticle or particle-wall overlaps can be interpreted as local material deformations. Overall, three different types of interaction models have been applied:

- particle–particle—interaction between primary particles. This model is applied between all primary particles even if they are connected with solid bonds;
- particle-wall—interaction between particles and compression walls;
- solid bonds—describes forces, moments and torques acting in single solid bond.

Due to the almost ideal elastic properties of UHPC, a linear elastic contact model was used for the particle–particle contact, while the Hertz-Mindlin model[26] was used for the particle-wall contact.

With respect to the interparticle interaction, force vector is decomposed in a normal and tangential part, respectively. In normal direction, the total force $\vec{F}_{n,total}$ is calculated by:

$$\vec{F}_{\mathrm{n,total}} = \vec{F}_{\mathrm{n}} - \vec{F}_{\mathrm{n,damping}}, \tag{1}$$

$$\vec{F}_{\mathrm{n}} = \mathrm{k_n} \cdot u_{\mathrm{n}} \cdot \vec{r}_{\mathrm{n}}, \tag{2}$$

$$\vec{F}_{\mathrm{n,damping}} = 1.8257 \cdot \alpha \cdot \left|\vec{v}_{\mathrm{rel,n}}\right| \cdot \sqrt{k_{\mathrm{n}} \cdot M^*} \cdot \vec{r}_{\mathrm{n}}, \tag{3}$$

$$\alpha = \frac{\ln(\mathrm{e})}{\sqrt{\pi^2 + \ln^2(\mathrm{e})}}, \mathrm{M}^* = \frac{\mathrm{m_1\, m_2}}{\mathrm{m_1 + m_2}} \text{ and } \vec{\mathrm{r}}_{\mathrm{n}} = \frac{\vec{\mathrm{P}}_1 - \vec{\mathrm{P}}_2}{\left|\vec{\mathrm{P}}_1 - \vec{\mathrm{P}}_2\right|}, \tag{4}$$

where k_{n} denotes the particle stiffness in normal direction, e is the restitution coefficient between two particles and $\vec{r}_{\mathrm{n}}$ the normalized contact vector between their centers $\vec{P}_1$ and $\vec{P}_2$, u_{n} the overlap, $\vec{v}_{\mathrm{rel,n}}$ the relative velocity and M^* the equivalent mass of the corresponding particles with the masses m_1 and m_2. The total force $\vec{F}_{\mathrm{t,total}}$ in tangential direction is further calculated by:

$$\vec{F}_{\mathrm{t,total}} = \vec{F}_{\mathrm{t}} - \vec{F}_{\mathrm{t,damping}}, \tag{5}$$

$$\vec{F}_{\mathrm{t}} = \vec{F}_{\mathrm{t,prev}} + k_{\mathrm{t}} \cdot \vec{u}_{\mathrm{t}}, \tag{6}$$

$$\vec{F}_{\mathrm{t,damping}} = 1.8257 \cdot \alpha \cdot \vec{v}_{\mathrm{rel,t}} \cdot \sqrt{k_{\mathrm{t}} \cdot M^*}, \tag{7}$$

where k_{t} denotes the particle stiffness in tangential direction, $\vec{F}_{\mathrm{t,prev}}$ the tangential force from the previous iteration, $\vec{u}_{\mathrm{t}}$ the increment of the tangential overlap in the current time step and $\vec{v}_{\mathrm{rel,t}}$ the relative velocity of the interacting particles. In addition, $\vec{F}_{\mathrm{t}}$ is limited by an interparticle friction linked with the sliding friction μ_{sl}:

$$\left|\vec{F}_{\mathrm{t}}\right| \le \mu_{\mathrm{sl}} \cdot \left|\vec{F}_{\mathrm{n}}\right|. \tag{8}$$

If Equation (8) is not fulfilled, than $\vec{F}_{\mathrm{t}}$ from Equation (6) is corrected to $\vec{F}_{\mathrm{t,cor}}$ according to Equation (9):

$$\vec{F}_{\mathrm{t,cor}} = \mu_{\mathrm{sl}} \cdot \left|\vec{F_n}\right| \cdot \frac{\vec{F}_{\mathrm{t}}}{\left|\vec{F}_{\mathrm{t}}\right|}. \tag{9}$$

Solid bonds between primary particles are modeled as ideally cylindrical objects with an initial length L_{init} and radius R_{b}, while latter cannot exceed the minimal radius

of contact partners. Here the elastic bond formulation[6,27] has been extended with additional damping forces in the normal and tangential direction. One of the challenges related to the usage of elastic bond model is almost non-damped oscillations during simulations. To reduce this effect artificial damper was added.

Generally, the stress acting on a bond is a result of the interaction between the corresponding particles. In order to simulate material breakage, stresses acting in each individual bond are analyzed and compared with the specified material properties for tension/compression strength σ_{max}, as well as tangential strength τ_{max}. If one of the conditions in Equations (10) or (11) is fulfilled, the bond breaks and is removed from the simulation:

$$\frac{F_{t,b}}{A_b} + M_{t,b} \cdot \frac{R_b}{I_{T,b}} > \tau_{max}, \tag{10}$$

$$\frac{F_{n,b}}{A_b} + M_{n,b} \cdot \frac{R_b}{J_b} > \sigma_{max}, \tag{11}$$

where $F_{t,b}$ and $F_{n,b}$ is the resulting force in normal and tangential direction, respectively. $M_{t,b}$ and $M_{n,b}$ is the torsional and bending moment acting on the bond, A_b and R_b the crosscut surface and radius, J_b the moment of inertia and $I_{T,b}$ the torsional moment of inertia.

3.3 | Basics of algorithms for model generation

In order to generate a coherent material structure of bonded particles, various algorithms and steps are required and will be described in the following. The application of the algorithms to generate the UHPC model is described in Section 4.

Particle generation algorithm

In the first step, a homogeneous packing of primary particles is generated. For this purpose, a force-biased algorithm was applied.[28] Initially, particles are randomly placed into a specified volume. After this, contacts between particles are detected and virtual forces in normal direction are calculated. Using the calculated forces, particles are moved while overlaps are reduced. The artificial stiffness which is used for calculating the interparticle forces is not related to the material properties, but calculated automatically from the maximum particle velocity in the generated system. In order to ensure that all particles are contained in the specified volume, virtual walls are generated. The packing algorithm stops when a specified overlap or a maximum number of iterations is reached.

Bond generation algorithm

In a next step, bonds can be generated between primary particles. For this purpose, a distance-based algorithm is used. A bond is generated if there is an interparticle overlap or if the distance between particle surfaces is smaller than a specified threshold. For cementitious materials, threshold distance was specified as 75% of particle diameter, in order to reach good connectivity of primary particles and capture the effect of interlocking.[15]

Agglomerate generation and placing

Using the described algorithms for particle and bond generation, it is possible to create agglomerates (particle clusters connected with bonds) which can be saved separately into the database of the MUSEN framework. Agglomerates can for instance be used to represent an additional material of a multiphase material system. The placing of these agglomerates into a specified volume follows an overlap-based algorithm, where a defined amount of agglomerates is randomly generated one by one. Afterwards, possible overlaps with already existing agglomerates are analyzed. If overlaps are detected, then the last agglomerate is removed from the domain and the iteration is repeated.

Material allocation algorithm

The material allocation algorithm is an approach for comparing particle positions using their coordinates. With respect to this contribution, particles of two separate volumes with different materials need to be compared and merged to a resulting volume. If the distance between the centers of two compared particles is within a specified limit R_{Limit}, corresponding particles are identified and the material is changed. In Figure 4, a particle allocation and the corresponding final particle arrangement with changed materials are shown schematically.

4 | GENERATION OF STRUCTURAL MODELS AND CALIBRATION OF PARAMETERS

4.1 | Binder and ITZ

Using the described approach for generation of structural models, cylindrical binder specimens with the dimensions of h/d = 72/24 mm were modeled. Keeping the h/d-ratio from experiments constant plays a major role, since effects like the obstruction of transverse strain may affect simulation results. Binder particles and bonds have a diameter of 0.48 mm, respectively. The chosen particle diameter leads to a total number of nearly 322,000 particles, while a threshold of −0.1 to +0.36 mm for bond

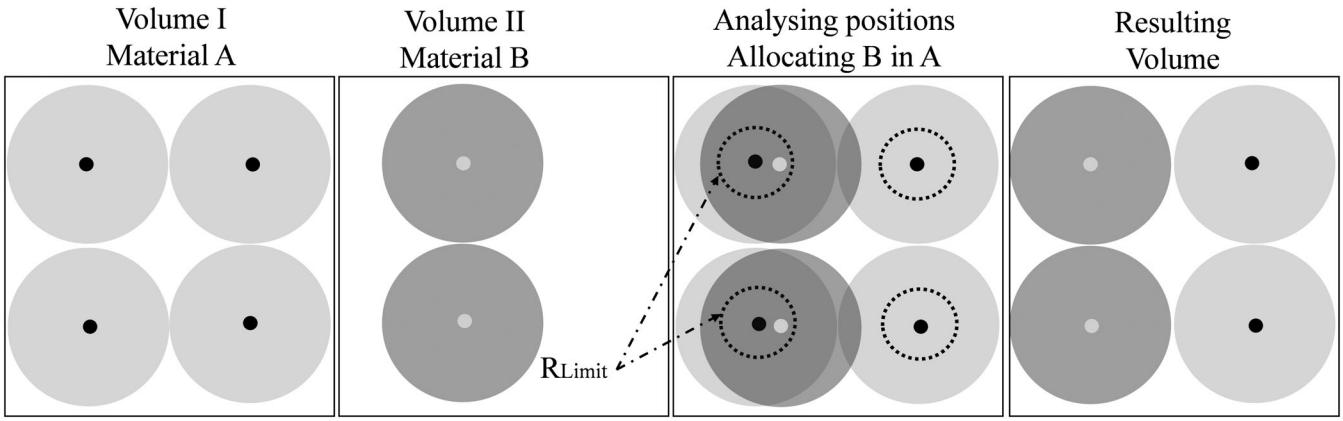

FIGURE 4 Schematic illustration of the particle allocation algorithm for two different materials

generation results in almost 3.63 million bonds. Two cylindrical plates were generated at the top and the bottom of the modeled specimen and set to loading velocities of zero and 100 mm/s, respectively. To speed up numerical simulations, compression velocity has been increased compared to the experimental results. By a velocity variation was ensured, that the increased value has no effect on simulation results. With respect to the calibration of model parameters, static compression tests on binder from Section 2 have been used. To reproduce the stiffness scattering of experimental data and to investigate the influence of a lower binder stiffness on the mechanical behavior of UHPC, a second parameter set was calibrated (by reducing the bond stiffness only). The calibrated parameters of set (A) correspond to the upper value of experimental data (38 GPa), while the parameter set (B) was calibrated to represent the experimental stiffness of 34 GPa, see Figure 5. Note that parameters of set (A) were further used as default values for simulations. An overview of final parameters is given in Table 3.

After the calibration of parameters, fracture patterns from simulations were compared with experiments. Generally, strongly pronounced vertical cracks and a formation of large fragments can be noticed. Several main fault zones have been formed and almost all of them are approximately perpendicular to the loading direction. Even if the mesoscopic simulation represents a small section of the macroscopic binder specimen, good agreements of the characteristic crack propagation and fracture patterns could be reached, see Figure 6a,b.

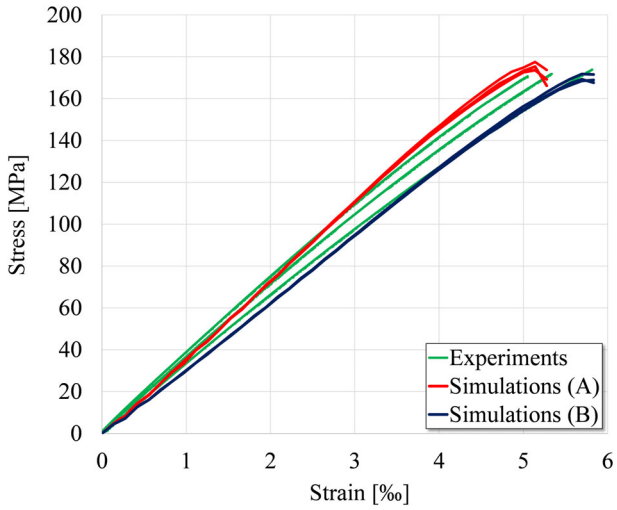

FIGURE 5 Comparison of binder experiments and six different binder simulations, red: Parameter set (a) for an experimental stiffness of 38 GPa, blue: Parameter set (b) for an experimental stiffness of 34 GPa

4.2 | Aggregate

All components of the concrete composition with small diameters, such as silica fume (200 nm) or quartz powder (20 μm), were incorporated into the binder. Only quartz aggregates (diameter 250 μm) which are large enough for meso scale modeling has been described separately. To consider the realistic nonspherical shape of aggregate in UHPC simulations, reconstructed 3D models from Section 2 were used and scaled to a diameter of around 4 mm. This μCT reconstruction can be used effectively for generation of BPM.[6,17,18,29,30] Primary particles with a diameter of 0.48 mm were placed into five segmented volumes, afterwards connected with bonds and saved into the MUSEN database, see Figure 7. To reproduce shape of aggregates and to ensure resulted force rearrangement between aggregate and binder in simulations, 500 to 1,000 particles were used for each agglomerate.

For the sake of simplicity, numerical calibration of aggregate parameters was carried out on cylindrical specimens under uniaxial compression. Two different

TABLE 3 Main simulation and material parameters from the calibration

Main simulation parameters	Binder	ITZ	Aggregate
Diameter of particles and bonds (mm)	0.48	0.48	0.48
Number of primary particles (–)	208,125	–	118,687
Number of solid bonds (–)	2,053,425	554,082	1,031,387
Simulation time step (s)	4e–10	4e–10	4e–10
Particle Young's modulus (GPa)	87.26	–	30
Bonds Young's modulus (GPa) Bond Young's modulus set (B) (GPa)	10 8	10 8	40 25
Normal and tangential stiffness k_n/k_t (N/m)	8.47e + 06	–	8.47e + 06
Bond normal strength (MPa)	6.72	6.72	∞
Bond tangential strength (MPa)	17.92	17.92	∞
Poisson number (–)	0.19	0.19	0.135
Interparticle sliding friction μ_{sl} (–)	0.45	–	0.45

Abbreviation: ITZ, interfacial transition zone.

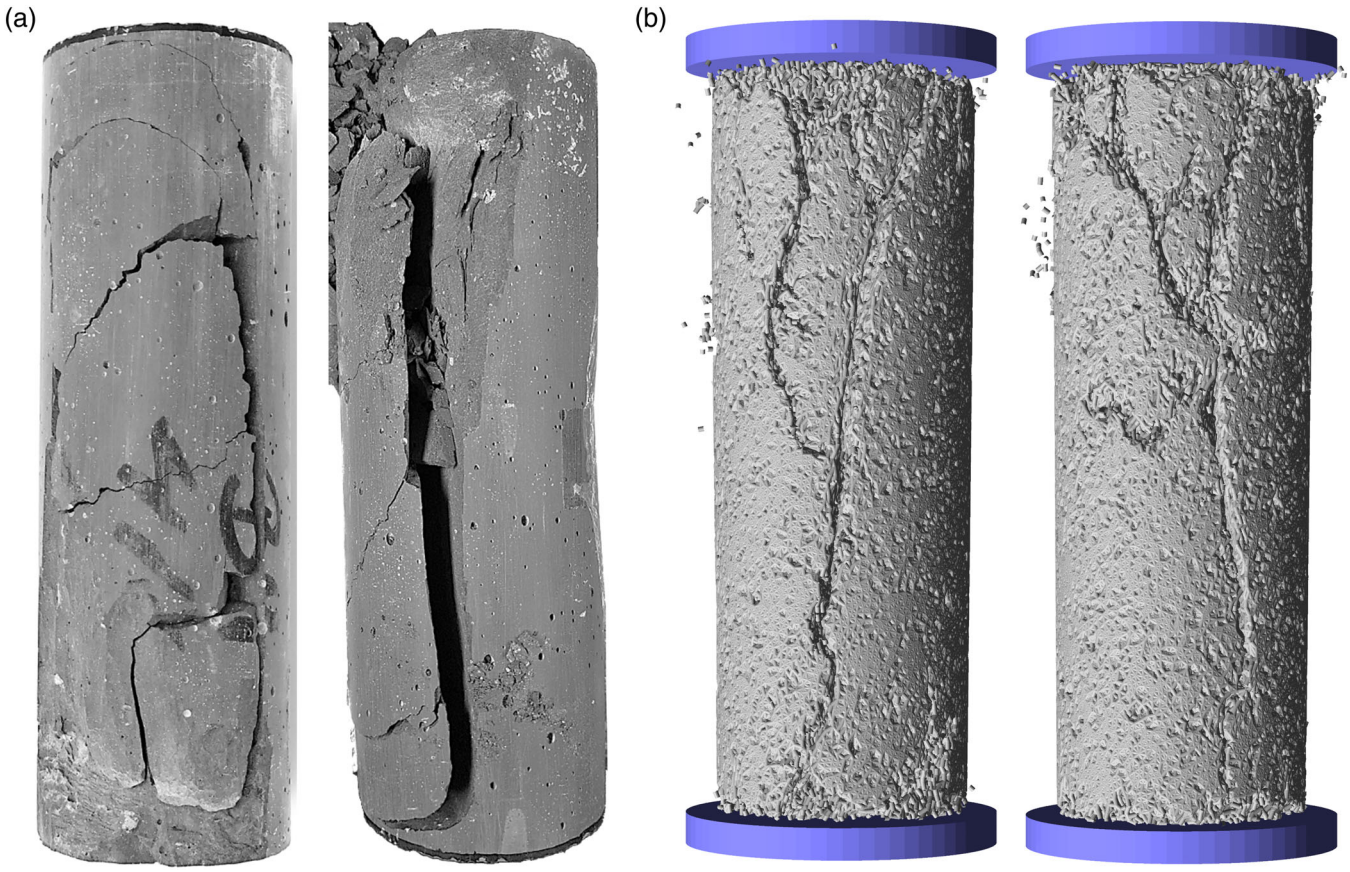

FIGURE 6 Comparison of fracture patterns for pure binder specimens: (a) Experiments and (b) simulations

parameter sets were calibrated. Parameters of set (A) correspond to a macroscopic stiffness of 90 GPa, while parameter set (B) refers to 70 GPa (see Section 2.2). Note that parameters of set (A) were further used as default values for simulations. As cracks were not penetrating the single grains in experiments, tangential and normal bond strength for aggregates was set to ∞. The infinite strength leads to a decrease of needed particle and bond stiffness in simulations, since broken bonds also affect the macroscopic stiffness (stiffness of modeled

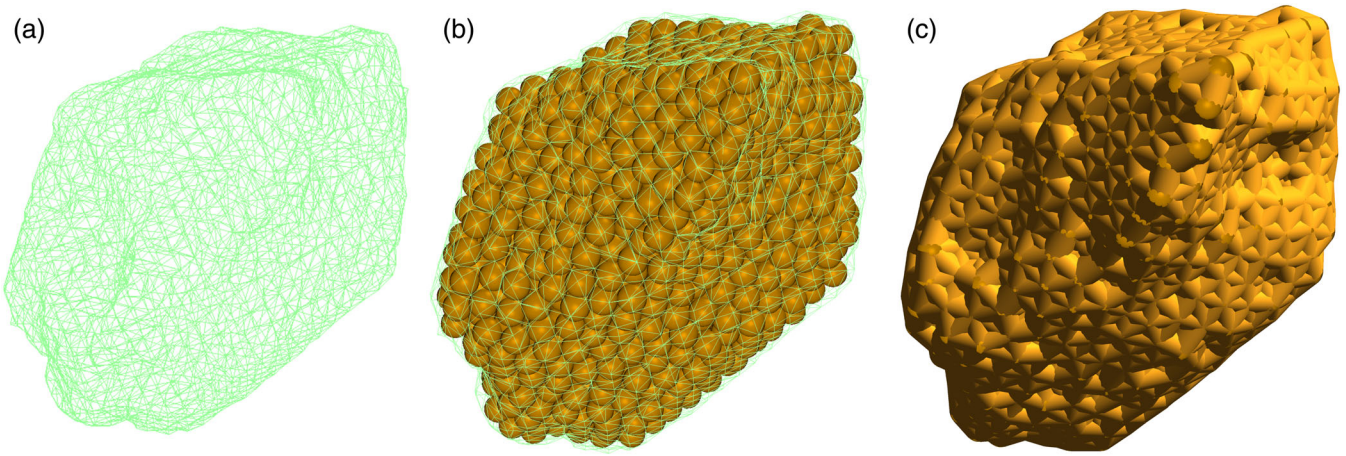

FIGURE 7 Usage of μCT data for agglomerate generation: (a) Polygon mesh of aggregate surface obtained from μCT measurements, (b) grain volume filled with aggregate particles, (c) BPM of single aggregate grain (aggregate agglomerate). BPM, bonded-particle model

cylinder). An overview of the calibrated parameters is given in Table 3.

4.3 | Structural three-phase UHPC model

The structural three-phase UHPC model consists of two types of particles (binder and aggregate) and three types of bonds (binder–binder, binder-aggregate and aggregate-aggregate). This three types of bonds represent the main three phases of concrete (binder, ITZ and aggregate) and allow to distinguish and analyze different sections of the modeled UHPC. Note, that due to the optimized packing density of the used UHPC, a potentially weaker ITZ was not observed in SEM investigations. For this reason, parameters of ITZ and binder bonds were assumed to be equal. The generation of the three-phase UHPC structure can be split into three main steps and corresponds to the algorithms mentioned in Section 3.3.

In the first step, binder particles and aggregate agglomerates are placed in two separate cylindrical volumes with the same dimensions (h/d = 72/24 mm). Based on the aggregate scaling, these dimensions represent a real concrete volume of around h/d = 6/2 mm. The particle number N was 326,812 for binder and 118,687 for aggregate particles by using the same particle diameter of $d_{binder/aggregate} = 0.48$ mm.

Afterwards, all positions of aggregate particles were allocated within the set of binder particles. After allocation the structure consists of 208,125 binder and 118,687 aggregate particles. The volumetric proportions of binder and aggregate are in accordance with the experimental UHPC composition from Table 1. Due to the identical particle diameter, particle numbers can be used for volumetric calculations, see Equations (12) and (13).

$$\frac{N_{binder}}{N_{particle,all}} = \frac{208,125}{326,812} = 63.68\,\text{Vol}\%. \quad (12)$$

$$\frac{N_{aggregate}}{N_{particle,all}} = \frac{118,687}{326,812} = 36.32\text{Vol}\%. \quad (13)$$

In the last step, all three types of bonds were generated. Note that all calibrated models had the same particle and bond diameter as well as the same coordination number. Due to this, the same threshold distance could be used for all materials during bond generation. Finally, two cylindrical plates were generated at the top and the bottom of the modeled specimen and set to loading velocities of 100 mm/s and zero, respectively. The stepwise generation is illustrated in Figure 8, as Table 3 contains a summary of the calibrated material parameters. Note, that these parameters are model parameters and thusly not equal to macroscopic data. The parameters of interparticle friction μ_{sl} were not included into the model calibration strategy and were assumed to be equal between all particles.

5 | UHPC SIMULATIONS

5.1 | Uniaxial compression

In the first stage the model parameters for binder, ITZ and aggregate have been calibrated using gradient-based trial and error principle. The calculations were iteratively repeated using different parameters to minimize discrepancy between experimental and numerical results. To estimate initial parameter set and to reduce number of iterations the linearization-based technique[31] has been used additionally.

Afterwards, using the calibrated parameters for single components such as binder, ITZ and aggregate,

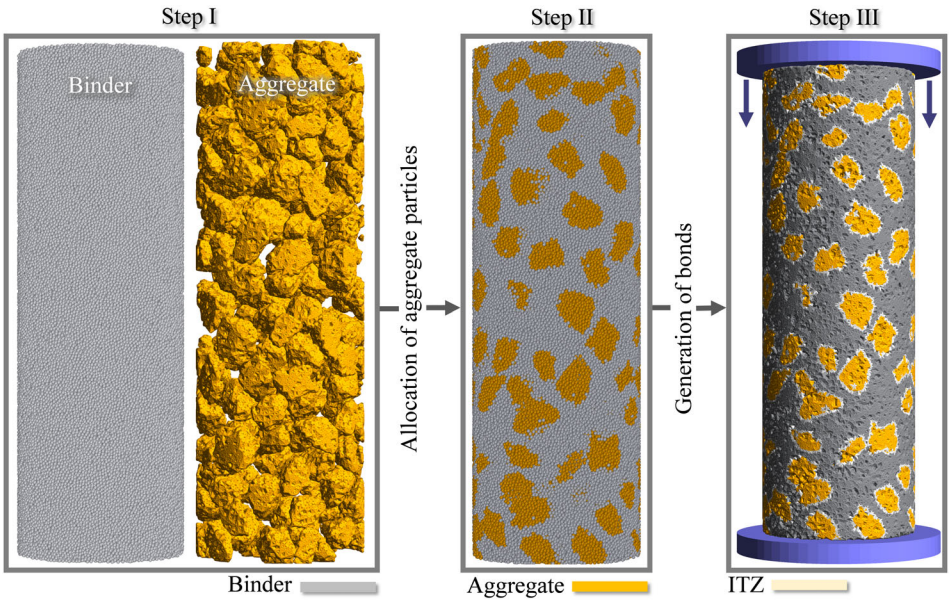

FIGURE 8 Stepwise generation of the three-phase concrete model. ITZ, interfacial transition zone

uniaxial compression of UHPC was simulated and validated with experimental data. Three separately generated samples with an aggregate content of around 36% were calculated. As it can be observed from comparison of stress–strain diagrams (Figure 9), good agreement between experimentally and numerically results could be reached.

Similarly to the binder samples, fracture patterns of concrete samples showed significant vertical cracks. In addition, more horizontal cracks could be noticed. This interaction during crack propagation affects a higher branching and forming of fragments. The formation of these fragments seems to be caused by additional aggregate, as cracks do not penetrate the single grains and are deflected around the grain. Even if the mesoscopic simulation represents a small section of the macroscopic concrete specimen from the experiments, good agreements of the characteristic crack propagation and fracture patterns could be reached. Note, that due to an explosive and abrupt failure of UHPC during experiments, specimens were additionally wrapped into a thin foil to keep the fracture fragments together as can be seen in Figure 10.

In order to localize the main crack initiation of the investigated UHPC, the particle stress distribution in loading direction was analyzed. The stress tensor acting on primary particles was calculated as[32]

$$\sigma_{i,j} = \frac{1}{2V_p}\sum_{K} l_i \cdot F_j, \tag{14}$$

where V_p is the particle volume, K is the total number of contacts for this particle including particle–particle

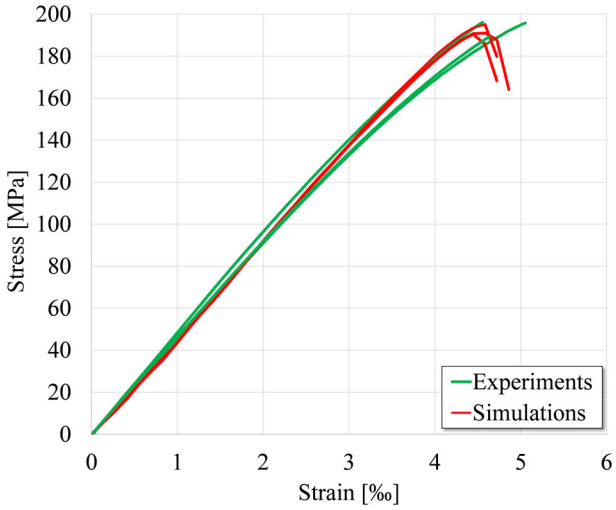

FIGURE 9 Comparison of UHPC experiments and three different UHPC simulations using calibrated parameters. UHPC, ultrahigh performance concrete

interactions and solid bonds, F_j is the force acting in specific contact, and l_i is the contact vector (connecting the particle centers) in the spatial directions i and j.

Particle stresses within the binder for UHPC sample (UHPC-Binder) were compared with the stress distribution acting in pure binder sample (binder–binder). Figure 11 displays distributions of the stress exerted under loads of I = 50, II = 100, and III = 150 MPa, respectively. All distributions take the shape of symmetrical bell curves. At higher macroscopic loads, the distributions become increasingly broad and shift toward higher individual particle stress.

In the case of the pure binder samples, these distributions are centered around the macroscopic load, but

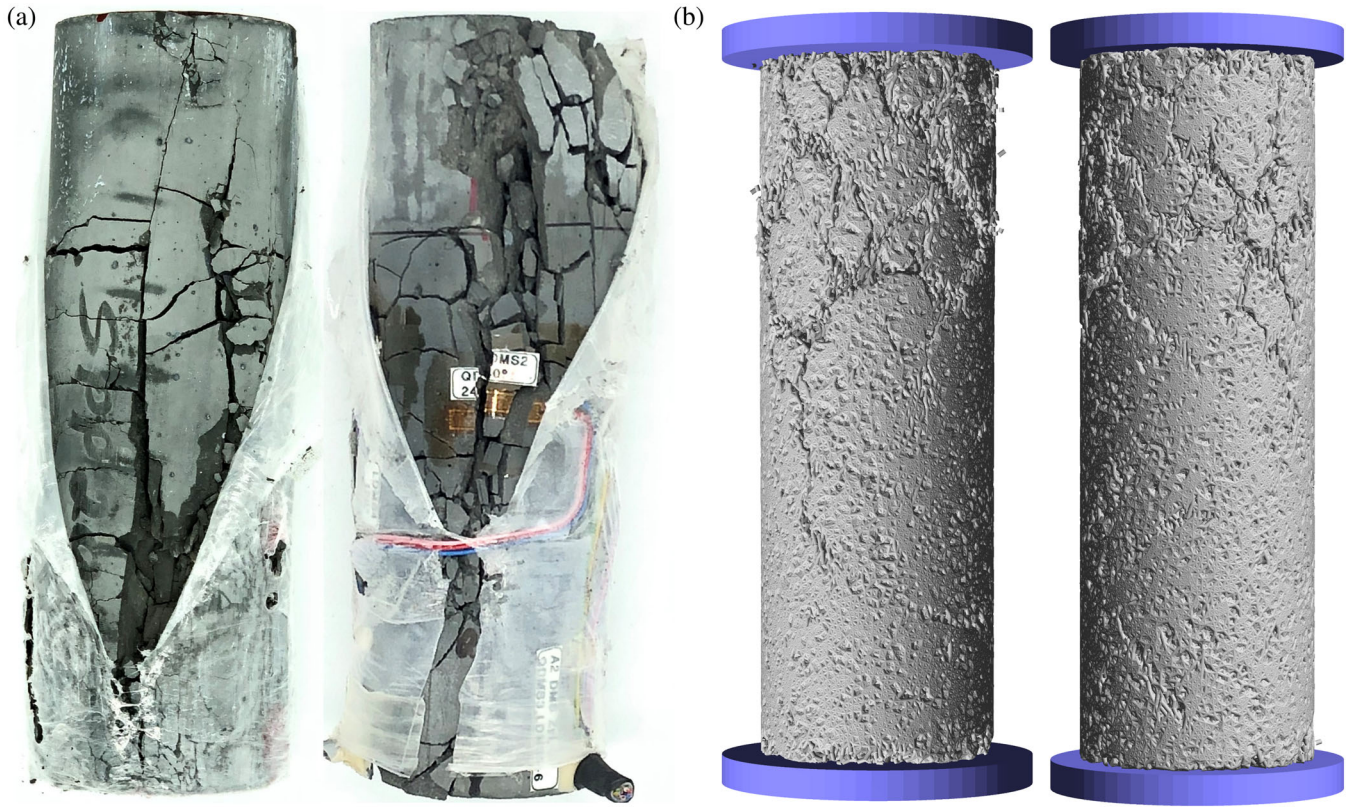

FIGURE 10 Comparison of the fracture patterns for UHPC: (a) Experimental specimens wrapped into a thin layer of foil and (b) resulting fracture patterns from DEM simulations. DEM, discrete element method; UHPC, ultrahigh performance concrete

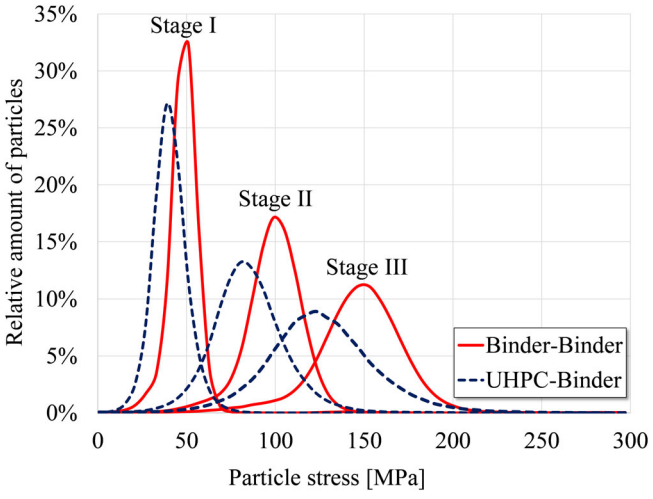

FIGURE 11 Stress distribution in loading direction for different loading stages [I = 50 MPa, II = 100 MPa, III = 150 MPa]: (red) pure binder simulation (binder–binder) from Section 4; (blue) binder particles for UHPC sample (UHPC-binder). UHPC, ultrahigh performance concrete

in the case of UHPC samples, the majority of particles is subjected to lower individual stress. In addition, UHPC generally exhibits broader and flatter distributions compared to the aggregate-free binder. As displayed in Figure 12c, particles subjected to a high-individual stress are mostly located between close-knit grains. Conversely, the stress exerted on particles is much lower in regions of binder containing no aggregate grains, see Figure 12b. Both effects can be explained by the additional presence of aggregate. On the one hand, grains absorb inner stresses and contribute to an increase of macroscopic strength as well as affect the shifted distribution of UHPC. On the other hand, discontinuities caused by the high difference of stiffness induce stress peaks, which can also lead to a higher local degradation of material.

Furthermore, evaluation of average bond stresses shows that the aforementioned stress peaks result in higher stresses within the ITZ bonds (Figure 13a) and lead to a higher amount of defects. This number of defects is the quantity of broken bonds to its initial number. Bond breakage at the meso level can be seen as a microcrack which is induced by mechanical load. It can be clearly noticed that the number of broken bonds has an exponential growth after passing a strain of 1.5%. From this point up to the average breakage strain of $\approx 4.5‰$, cracks are clearly dominated by the failure of ITZ bonds, see Figure 13b.

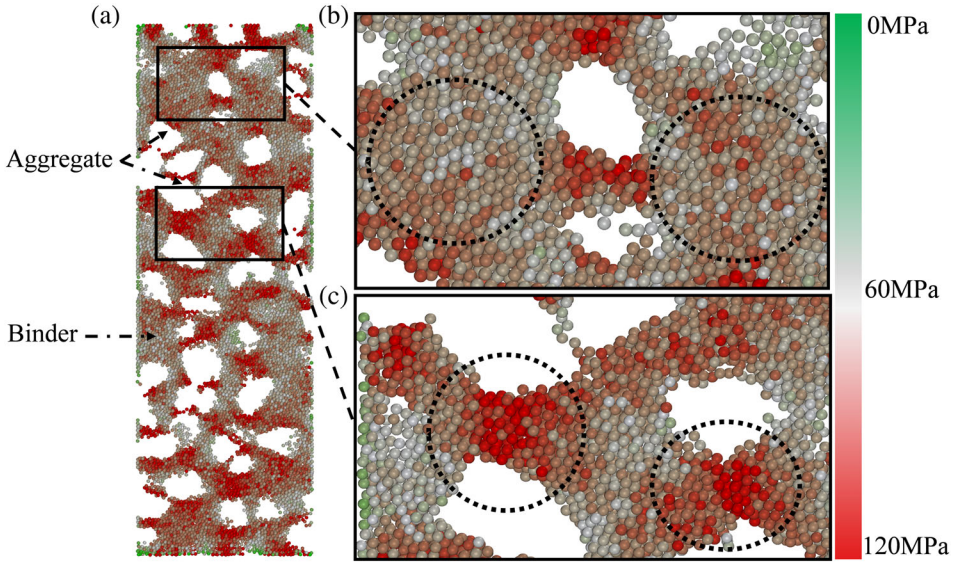

FIGURE 12 Stresses of primary binder particles in loading direction at strain level of 2%: (a) Main visualization of stress peaks in the simulated specimen, (b) lower stresses in aggregate-free areas, and (c) higher stresses in regions of close-knit grains

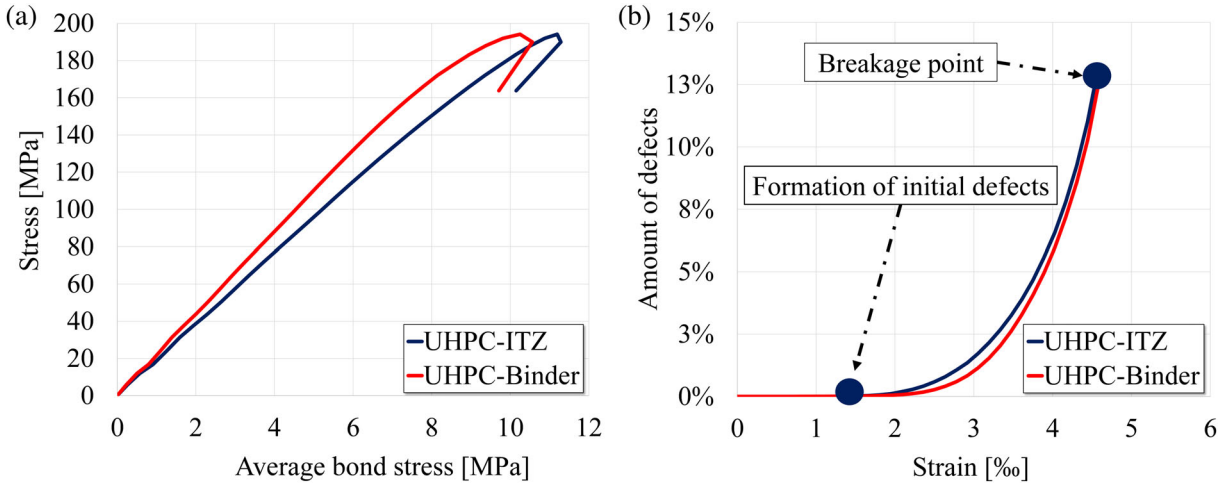

FIGURE 13 Comparison between ITZ and binder bonds: (a) Higher degradation of ITZ bonds caused by higher stresses and (b) defect propagation within the simulated UHPC structure. ITZ, interfacial transition zone; UHPC, ultrahigh performance concrete

5.2 | Uniaxial compression with varied aggregate content

By a variation of aggregate content, changes in the mechanical behavior of UHPC were investigated. This can be used for an optimization of the particle distribution of the concrete composition or to point out the influence of local inhomogeneities caused by an insufficient mixing procedure. An optimization of concrete composition usually affects the entire distribution and influences the processability as well as the optimized packing density. For this reason, the increase of aggregate content was limited to 50%, as otherwise potentially unrealistic scenarios would be reproduced. The simulation results under uniaxial compression with varied aggregate content are shown in Table 4 and plotted in Figure 14.

It can be clearly noticed that an increase of aggregate content leads to a significant increase of stiffness and strength, respectively. Simulations with an aggregate content between 30% and 40% correspond well with the experimental data (see Table 2). An aggregate content of 30% results in an average strength of 187 MPa and stiffness of 44 GPa (lower value of experiments: 188 MPa/46 GPa), while a content of 40% increases the strength to 196 MPa and the stiffness to 47 GPa (higher value of experiments: 196 MPa/48 GPa). These results reflect well the strong influence of aggregate concentration in UHPC, which was for example, mentioned by Jang et al., and Zhang et al.[33,34] In contrast to plain concrete, the optimized packing density as well as the high-strength ITZ of UHPC lead to a homogeneous structure where stresses can be borne by both, binder and

aggregate. Furthermore, simulations showed a linear correlation between aggregate content and Young's modulus, while a quadratic relation between aggregate and strength was found. The dependency can be described with the following functions:

$$E_c = 0.25 \cdot a_c + E_B, \tag{15}$$

$$f_c = 0.8 \cdot a_c^2 + 0.18 \cdot a_c + f_B, \tag{16}$$

TABLE 4 Simulation results for varied aggregate content

Volumetric aggregate content (%)	Young's modulus of UHPC (GPa)	Compressive strength of UHPC (MPa)
0	36.87 ± 0.14	175.48 ± 1.64
10	38.94 ± 0.39	176.90 ± 0.94
20	41.73 ± 0.32	180.27 ± 0.81
30	44.26 ± 0.38	187.27 ± 0.97
36	45.78 ± 0.29	192.15 ± 2.09
40	46.62 ± 0.17	196.15 ± 1.34
45	48.04 ± 0.17	199.32 ± 1.09
50	49.05 ± 0.14	202.25 ± 0.43

Abbreviation: UHPC, ultrahigh performance concrete.

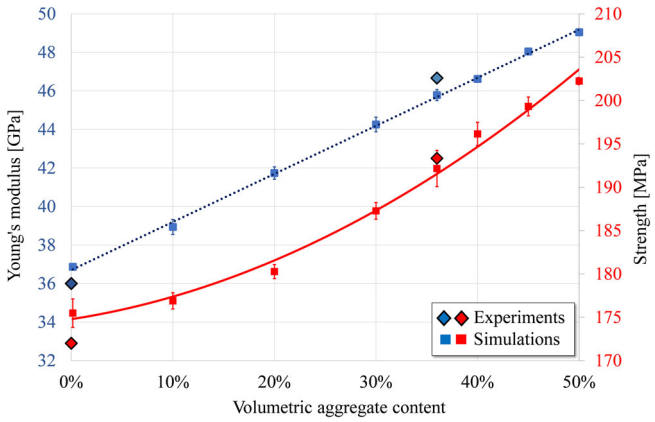

FIGURE 14 Influence of aggregate content on Young's modulus and compressive strength

where a_c is the aggregate content in Vol-%, E_B and E_c the modulus of elasticity of binder and concrete and f_c as well as f_b the strength of concrete and binder. Similar trends for a linear correlation between aggregate content and the modulus of elasticity have been observed in experimental investigations of Cho et al.[35] for different concrete compositions and varied w/c ratios. Moreover, the quadratic correlation is in accordance with experimental conclusions of Stock et al.[36] in which effects of aggregate concentration on the mechanical properties of concrete were investigated.

5.3 | Uniaxial compression with varied aggregate and binder stiffness

In order to determine the influence of binder and aggregate stiffness on the mechanical properties of UHPC, material parameters were changed to the parameter set (B). These parameters were calibrated to investigate the influence of aggregate anisotropy and scattering of binder stiffness within experimental data, as mentioned in Sections 4.1 and 4.2. Three simulations were performed with each combination of parameter set. Table 5 contains the used combinations and obtained results from simulations, where parameter set (B) represents the lower stiffness value.

While a 22% decrease in aggregate stiffness (from 90 to 70 GPa) causes a drop in concrete stiffness of only 7% (from 45 to 42 GPa), a smaller decrease in binder stiffness of only 11% (from 38 to 34 GPa) brings about a similar drop in concrete stiffness. At the same time, concrete strength is not noticeably influenced by a decrease in stiffness of either component. Similar trends have been observed by experimental investigations of Aïtcin et al. and Zhou et.al. [37,38] for high-performance concrete, where different aggregate types were used for stiffness variation. In addition Zhou et.al,[38] observed a discontinuous influence of aggregate stiffness, where concrete strength is constant within certain intervals of aggregate stiffness and only varies significantly upon drastic variations in aggregate stiffness. From these results, we conclude that the main contributing factor in the high

TABLE 5 Combination of parameter sets and the corresponding simulation results

Combination	Parameter set of binder/ITZ	Parameter set of aggregate	Young's modulus of UHPC (GPa)	Strength of UHPC (MPa)
I (default)	(A)	(A)	45.78 ± 0.53	192.15 ± 2.09
II	(A)	(B)	42.15 ± 0.13	192.70 ± 3.43
III	(B)	(A)	42.10 ± 0.54	191.06 ± 2.84

Abbreviations: ITZ, interfacial transition zone; UHPC, ultrahigh performance concrete.

strength of UHPC is the binder and the optimized packing, while the aggregate stiffness plays a secondary role.

6 | CONCLUSION

This paper presented a numerical study of the mechanical behavior of UHPC based on DEM, X-ray μCT, SEM as well as PLM. It was shown that the characteristic attributes of UHPC may be accurately modeled using the BPM approach. The mesoscopic three-phase BPM proved to be a beneficial approach that gives insight into the mechanical processes within the UHPC structure and to localize main crack initiation factor. Even though no weaker ITZ was identified by SEM–EDX line-scans, it is advisable to use transition bonds for a clear distinction of different material sections. Based on our numerical analyses of the investigated UHPC composition, which we directly compared to corresponding experiments, the following main conclusions may be drawn:

- The main contributing factor in the high strength of the investigated UHPC is the binder with its optimized ITZ and an appropriate packing density. Only for this it is possible, that stresses can be relieved by both binder and aggregate.
- Local discontinuities in stiffness (caused by the high stiffness of aggregate and especially in case of grains close to each other) lead to stress peaks around the grains and thusly to a higher degradation of the directly surrounding binder.
- Crack initiation and propagation have an exponential growth and the failure is dominated by ITZ bonds, even though the transition zone has the same properties as the overall binder matrix. This is a consequence of the stress concentrations around the aggregate which are induced into ITZ bonds.
- Different volumetric contents of aggregate lead to a change in strength and stiffness, respectively. These kind of inhomogeneities could further lead to an early local failure and influence the macroscopic behavior of experimental investigation, which shows the importance of a sufficient mixing procedure for UHPC.
- A decrease of aggregate or binder stiffness causes a decrease of concrete stiffness only. It is further conceivable that this effect overlaps with the influence from different aggregate contents and might lead to a higher scattering in experimental investigations.

ACKNOWLEDGMENTS

This research has been carried out within the priority program SPP2020 “Cyclic deterioration of High-Performance Concrete in an experimental-virtual lab” financed by the German Research Foundation (DFG) under the grants: DO 2026/2-1, RI 1516/2-1, SCHM 1473/29-1.

DATA AVAILABILITY STATEMENT

Research data are not shared

ORCID

Sebastian Rybczyński https://orcid.org/0000-0001-6786-2244
Maksym Dosta https://orcid.org/0000-0002-7578-8408
Gunnar Schaan https://orcid.org/0000-0001-9680-799X
Martin Ritter https://orcid.org/0000-0002-5664-859X
Frank Schmidt-Döhl https://orcid.org/0000-0003-3346-965X

REFERENCES

1. Arora A, Aguayo M, Hansen H, et al. Microstructural packing- and rheology-based binder selection and characterization for ultra-high performance concrete (UHPC). Cem Concr Res. 2018;103:179–190. https://doi.org/10.1016/j.cemconres.2017.10.013.
2. Wang X, Yu R, Song Q, et al. Optimized design of ultra-high performance concrete (UHPC) with a high wet packing density. Cem Concr Res. 2019;126:105921. https://doi.org/10.1016/j.cemconres.2019.105921.
3. Raheem AHA, Mahdy M, Mashaly AA. Mechanical and fracture mechanics properties of ultra-high-performance concrete. Constr Build Mater. 2019;213:561–566. https://doi.org/10.1016/j.conbuildmat.2019.03.298.
4. Abdulkareem OM, Fraj AB, Bouasker M, Khelidj A. Mixture design and early age investigations of more sustainable UHPC. Constr Build Mater. 2018;163:235–246. https://doi.org/10.1016/j.conbuildmat.2017.12.107.
5. Alkaysi M, El-Tawil S, Liu Z, Hansen W. Effects of silica powder and cement type on durability of ultra high performance concrete (UHPC). Cem Concr Compos. 2016;66:47–56. https://doi.org/10.1016/j.cemconcomp.2015.11.005.
6. Dosta M, Dale S, Antonyuk S, Wassgren C, Heinrich S. Numerical and experimental analysis of influence of granule microstructure on its compression breakage. Powder Technol. 2016;299:87–97. https://doi.org/10.1016/j.powtec.2016.05.005.
7. Potyondy DO. The bonded-particle model as a tool for rock mechanics research and application: Current trends and future directions. Geosyst Eng. 2015;18:1–28. https://doi.org/10.1080/12269328.2014.998346.
8. Cusatis G, Mencarelli A, Pelessone D, Baylot J. Lattice discrete particle model (LDPM) for failure behavior of concrete. II: Calibration and validation. Cem Concr Compos. 2011;33(9):891–905. https://doi.org/10.1016/j.cemconcomp.2011.02.010.
9. Donze F, Magnier S, Daudeville L, Mariotti C, Davenne L. Numerical study of compressive behavior of concrete at high strain rates. J Eng Mech. 1999;125(10):31154–31163. https://doi.org/10.1061/(ASCE)0733-9399(1999)125:10(1154).
10. Hentz S, Donze F, Daudeville L. Identification and validation of a discrete element model for concrete. J Eng Mech. 2004;130

(6):709–719. https://doi.org/10.1061/(ASCE)0733-9399(2004)130:6(709).
11. Kim H, Buttlar WG. Discrete fracture modeling of asphalt concrete. Int J Solids Struct. 2009;46:2593–2604. https://doi.org/10.1016/j.ijsolstr.2009.02.006.
12. Nitka M, Tejchman J. Modelling of concrete behavior in uniaxial compression and tension with DEM. Granular Matter. 2015;17:145–164. https://doi.org/10.1007/s10035-015-0546-4.
13. Poinard C, Piotrowska E, Malecot Y, Daudeville L, Landis E. Compression triaxial behavior of concrete: The role of the mesostructure by analysis of X-ray tomographic images. Eur J Environ Civ Eng. 2012;16(1):115–136. https://doi.org/10.1080/19648189.2012.682458.
14. Skarzynski L, Nitka M, Tejchman J. Modelling of concrete fracture at aggregate level using FEM and DEM based on X-ray μCT images of internal structure. Eng Fract Mech. 2015;147:13–35. https://doi.org/10.1016/j.engfracmech.2015.08.010.
15. Scholtès L, Donzé F-V. A DEM model for soft and hard rocks: Role of grain interlocking on strength. J Mech Phys Solids. 2013;61(2):352–369. https://doi.org/10.1016/j.jmps.2012.10.005.
16. Latham J-P, Munjiza A, Garcia X, Xiang J, Guises R. Three-dimensional particle shape acquisition and use of shape library for DEM and FEM/DEM simulation. Miner Eng. 2008;21(11):797–805. https://doi.org/10.1016/j.mineng.2008.05.015.
17. Garboczi EJ, Cheok GS, Stone WC. Using LADAR to characterize the 3-D shape of aggregates: Preliminary results. Cem Concr Res. 2006;36:1072–1075. https://doi.org/10.1016/j.cemconres.2006.03.017.
18. Kozhar S, Dosta M, Antonyuk S, Heinrich S, Bröckel U. DEM simulations of amorphous irregular shaped micrometer-sized titania agglomerates at compression. Adv Powder Technol. 2015;26:767–777. https://doi.org/10.1016/j.apt.2015.05.005.
19. Spettl A, Bachstein S, Dosta M, Goslinska M, Heinrich S, Schmidt V. Bonded-particle extraction and stochastic modeling of internal agglomerate structures. Adv Powder Technol. 2016;27:1761–1774. https://doi.org/10.1016/j.apt.2016.06.007.
20. Preibisch S, Saalfeld S, Tomancak P. Globally optimal stitching of tiled 3D microscopic image acquisitions. Bioinformatics. 2009;25(11):1463–1465. https://doi.org/10.1093/bioinformatics/btp184.
21. Pabst W, Gregorová E. Elastic properties of silica polymorphs-a review. Ceramics-Silikaty. 2013;57(3):167–184.
22. Peng Z, Redfern S. Mechanical properties of quartz at the α-β phase transition: Implications for tectonic and seismic anomalies. Geochem Geophys Geosyst. 2013;14(1):18–28. https://doi.org/10.1029/2012GC004482.
23. Cundall PA, Strack ODL. A discrete numerical model for granular assemblies. Geotechnique. 1979;29:47–65. https://doi.org/10.1680/geot.1979.29.1.47.
24. Dosta M, Skorych V. MUSEN: An open-source framework for GPU-accelerated DEM simulations. SoftwareX. 2020;12:100618. https://doi.org/10.1016/j.softx.2020.100618.
25. Iwai T, Hong CW, Greil P. Fast particle pair detection algorithms for particle simulations. Int J Modern Phys. 1999;10:823–837. https://doi.org/10.1142/S0129183199000644.
26. Mindlin RD, Deresiewicz H. Elastic spheres in contact under varying oblique forces. J Appl Mech. 1953;20(3):327–344.
27. Potyondy DO, Cundall PA. A bonded-particle model for rock. Int J Rock Mech Min Sci. 2004;41(8):1329–1364. https://doi.org/10.1016/j.ijrmms.2004.09.011.
28. Dosta M, Weber M, Schmidt V, Antonyuk S. DEM analysis of breakage behavior of bicomponent agglomerates. In: Antonyuk S, editor. Particles in contact. Cham: Springer, 2019. https://doi.org/10.1007/978-3-030-15899-6_6.
29. Spettl A, Dosta M, Antonyuk S, Heinrich S, Schmidt V. Statistical investigation of agglomerate breakage based on combined stochastic microstructure modeling and DEM simulations. Adv Powder Technol. 2015;26:1021–1030. https://doi.org/10.1016/j.apt.2015.04.011.
30. Wang P, Gao N, Ji K, Stewart L. DEM analysis on the role of aggregates on concrete strength. Comput Geotech. 2019;119:103290. https://doi.org/10.1016/j.compgeo.2019.103290.
31. Jarolin K, Dosta M. Linearization-based methods for the calibration of bonded-particle models. Comput Particle Mech. 2020. https://doi.org/10.1007/s40571-020-00348-z.
32. Tsoungui O, Vallet D, Charmet J. Numerical model of crushing of grains inside two-dimensional granular materials. Powder Technol. 1999;105:190–198. https://doi.org/10.1016/S0032-5910(99)00137-0.
33. Jang HO, Lee HS, Cho K. Experimental study on shear performance of plain construction joints integrated with ultra-high performance concrete (UHPC). Constr Build Mater. 2017;152:16–23. https://doi.org/10.1016/j.conbuildmat.2017.06.156.
34. Zhang Y, Zhang C, Zhu Y, Cao J, Shao X. An experimental study: Various influence factors affecting interfacial shear performance of UHPC-NSC. Constr Build Mater. 2020;236:117480. https://doi.org/10.1016/j.conbuildmat.2019.117480.
35. Cho S, Yang C, Huang R. Effect of aggregate volume fraction on the elastic moduli and void ratio of cement-based materials. Marine Sci Technol. 2000;8(1):1–7.
36. Stock AF, Hannant DJ, Williams RIT. The effect of aggregate concentration upon the strength and modulus of elasticity of concrete. Mag Concr Res. 1979;31(109):225–234. https://doi.org/10.1680/macr.1979.31.109.225.
37. Aïtcin PC, Mehta PK. Effect of coarse aggregate characteristics on mechanical properties of high-strength concrete. ACI Mater J. 1990;87(2):103–107.
38. Zhou FP, Lydon FD, Barr BIG. Effect of coarse aggregate on elastic modulus and compressive strength of high performance concrete. Cem Concr Res. 1995;25(1):177–186. https://doi.org/10.1016/0008-8846(94)00125-I.

AUTHOR BIOGRAPHIES

Sebastian Rybczyński, Hamburg University of Technology, Institute of Materials, Physics and Chemistry of Buildings, Hamburg, Germany.

Maksym Dosta, Hamburg University of Technology, Institute of Solids Process Engineering and Particle Technology, Hamburg, Germany.

Gunnar Schaan, Hamburg University of Technology, Electron Microscopy Unit, Hamburg, Germany.

Martin Ritter, Hamburg University of Technology, Electron Microscopy Unit, Hamburg, Germany.

Frank Schmidt-Döhl, Hamburg University of Technology, Institute of Materials, Physics and Chemistry of Buildings, Hamburg, Germany.

How to cite this article: Rybczyński S, Dosta M, Schaan G, Ritter M, Schmidt-Döhl F. Numerical study on the mechanical behavior of ultrahigh performance concrete using a three-phase discrete element model. *Structural Concrete*. 2020;1–16. https://doi.org/10.1002/suco.202000435